

# An analysis of the microstructures developed in experimentally deformed polycrystalline pyrite and minor sulphide phases using electron backscatter diffraction

Craig D. Barrie\*, Alan P. Boyle, David J. Prior

*Department of Earth and Ocean Sciences, University of Liverpool, Liverpool, L69 3GP, UK*

Received 9 January 2007; received in revised form 19 April 2007; accepted 14 May 2007

Available online 29 May 2007

## Abstract

Samples of polycrystalline pyrite previously deformed in tri-axial compression tests at a confining pressure of 300 MPa and a strain rate of  $2 \times 10^{-4} \text{ s}^{-1}$  but varying temperature were analysed in this study. Five samples including the original starting material have undergone analysis using foreshorter orientation contrast (OC) imaging coupled with electron back scatter diffraction (EBSD) to determine how the micro-structures in pyrite and to an extent the surrounding minor phases have changed with increasing temperature. Between 550 °C and 650 °C the dominant deformation mechanism in pyrite is that of dislocation creep. Above 650 °C this mechanism becomes less apparent and few if any dislocation walls are present within pyrite grains by 700 °C. This is a result of either increased dynamic recrystallisation with temperature or a change in the dominant deformation mechanism. Dislocation creep occurs via lattice rotation, principally about a single  $\langle 100 \rangle$  axis, but also about two separate  $\langle 100 \rangle$  axes and more rarely about a single  $\langle 110 \rangle$  axis. Deformation has not resulted in a crystallographic preferred orientation (CPO) within any of the samples. Shape change of pyrite grains has occurred and this can account for most if not all of the shortening applied, but dynamic recrystallisation of pyrite and grain boundary sliding accommodated along the minor phases are also likely to be important mechanisms in all of the samples.

© 2007 Elsevier Ltd. All rights reserved.

*Keywords:* Pyrite; Tennantite; Electron backscatter diffraction; Dislocation creep; Recrystallisation; Experimental deformation

## 1. Introduction

Pyrite is the most abundant sulphide mineral on Earth and an important phase in many economic ore bodies. Although pyrite is not typically of economical interest, its refractory nature means it is capable of preserving geological history not preserved in the softer economic sulphides such as chalcopyrite and galena. The preservation of early deformational features that occurred prior to the peak of metamorphic conditions are of significant importance. Many sulphide ore deposits form at plate margins (Allen et al., 2002) and often get involved in later orogenic events resulting in deformation and/or metamorphism

of the ores. Thus, understanding pyrite is key to understanding the genesis of ore bodies and how those which have undergone deformation have evolved through time.

The deformation mechanisms that operate in pyrite have been a topic of considerable interest. Early studies suggested that pyrite was a very hard mineral, which deformed by brittle mechanisms at all levels in the Earth's crust (Ramdohr, 1969; Gill, 1969; Graf and Skinner, 1970; Atkinson, 1975; Van Goethem et al., 1978). It was not until the work of (Graf et al., 1981) that plastic deformation was identified in pyrite and the work that followed (Cox et al., 1981; Levade et al., 1982; McClay and Ellis, 1983, 1984) suggested that the brittle-ductile transition in pyrite was at about 425 °C. In recent times, the use of new techniques such as neutron diffraction, SEM-based electron backscatter diffraction (EBSD) and foreshorter orientation contrast (OC) imaging has led to further

\* Corresponding author.

*E-mail address:* c.d.barrie@liverpool.ac.uk (C.D. Barrie).

study of the deformation mechanisms operating in pyrite (Siemes et al., 1993; Boyle et al., 1998), demonstrating that pyrite can deform plastically at lower greenschist facies conditions (Freitag et al., 2004), much lower temperature than proposed by the deformation mechanism map for pyrite (McClay and Ellis, 1983).

In this study we seek to characterize the deformation microstructures developed at the grain and sub-grain scale in polycrystalline pyrite and to an extent in the surrounding minor sulphides. Analysis was carried out by systematic study of four samples deformed at known pressure, temperature and strain rate in experiments by Cox et al. (1981), and an undeformed sample of the starting material. This allowed the validity of previous studies of the same samples to be tested, all of which have been limited to a certain extent by inherent assumptions due to the spatial resolution of the techniques used. This paper will initially summarise the previous work carried out on the samples and then describe the results of this study and its implications for pyrite micro-structural development and the pyrite deformation mechanism map (McClay and Ellis, 1983).

**2. Previous work**

The five samples in this study all come from a single block of fine grained polycrystalline pyrite (Table 1) from the Blow ore body of the Mt Lyell Mining and Railway Company near Queenstown, Tasmania. All samples were drilled out as cylinders (12 mm long, 7 mm dm) with the cylinder axes contained within a foliation defined by grain size and compositional layering within the ore. Four samples were deformed in a gas apparatus rig by tri-axial shortening (Cox et al., 1981) at a strain rate of  $2 \times 10^{-4} \text{ s}^{-1}$  and a confining pressure of 300 MPa (Fig. 1). The deformed samples were characterised using reflected light microscopy and transmission electron microscopy (TEM) and the results showed evidence for dislocation flow mechanisms as well as dynamic recrystallisation and recovery (Cox et al., 1981). These results were used by McClay and Ellis (1983) to constrain the strain-rate contours for dislocation glide and creep in their proposed deformation–mechanism map for pyrite (Fig. 2).

The same samples were analysed further by Siemes et al. (1993) using neutron diffraction texture goniometry analysis. This technique (Brokmeier, 1989; Siemes et al., 1993; Jansen et al., 1993) is a means of determining whether the grains in the samples have an overall crystallographic preferred

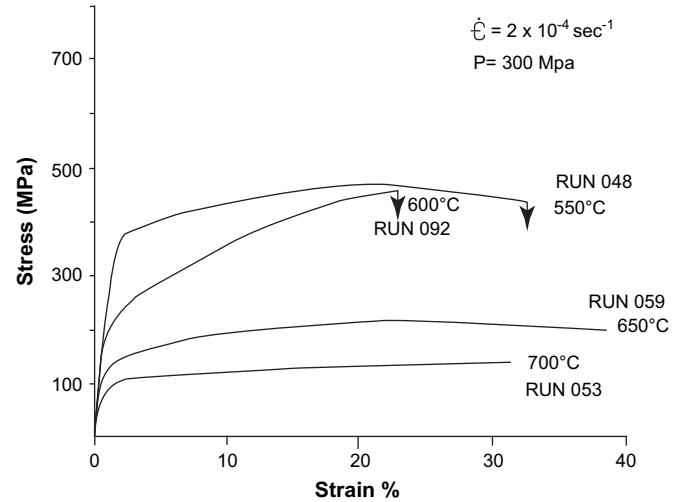


Fig. 1. Stress strain curves for the experimentally deformed pyrite with a confining pressure of 300 MPa and a strain rate of  $2 \times 10^{-4} \text{ s}^{-1}$ . The lowest temperature samples runs 048 and 092 failed before completion (adapted from Cox et al., 1981).

orientation (CPO). The results suggested that the original undeformed material (B-1) has a very weak  $\langle 111 \rangle$  fibre texture, which persists in all of the samples up to 700 °C. At 700 °C the  $\langle 111 \rangle$  fabric is apparently replaced by a new and weak  $\langle 100 \rangle$  texture, which forms parallel to the shortening direction. This variation in CPO is interpreted to indicate a change in the dominant flow mechanism as temperature reaches 700 °C (Siemes et al., 1993).

**3. Methods**

*3.1. Sample preparation*

All four experimentally deformed samples had been previously cut parallel to the experimental shortening direction

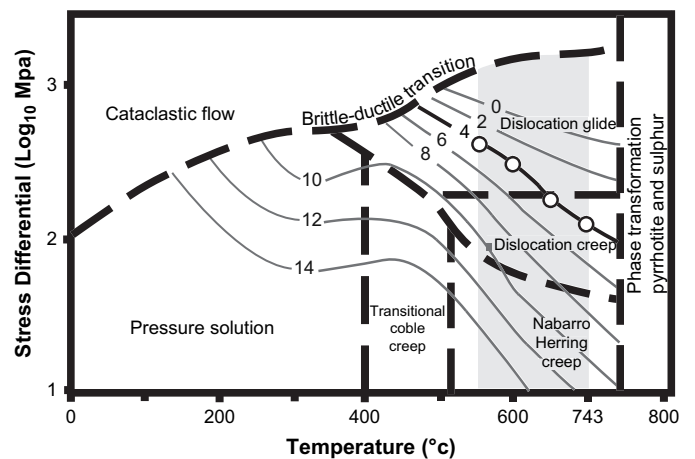


Fig. 2. The proposed deformation mechanism map for polycrystalline pyrite of 100  $\mu\text{m}$  grain size. Strain rate contours are in  $10^{-n} \text{ s}^{-1}$  and were defined using the results from deformation of the experimental samples in this study (McClay and Ellis, 1984). The  $2 \times 10^{-4} \text{ s}^{-1}$  strain rate contour is highlighted as is the temperature range of all four deformed samples.

Table 1  
Summary table listing the main minerals present within each sample and there approximate proportions

Sample no.	B-1	048	092	059	053
Temperature (°C)	N/A	550	600	650	700
Pyrite (%)	~95	~95	~95	~95	~95
Tennantite (%)	~4	~4	~2	~2.5	~2
Chalcopyrite (%)	<1	<1	~1	~2	~2
Barite (%)	<1	<1	~2	<1	~1

during earlier studies (Cox et al., 1981; Siemes et al., 1993). The starting material cylinder was cut both parallel ( $XY$  plane) and perpendicular ( $XZ$  plane) to the length of the cylinder (Fig. 3). All of the samples were mounted in resin blocks and mechanically polished before analysis was carried out. For EBSD work the samples were also polished on a polyurethane lap for 1 h using a suspension of  $0.05\ \mu\text{m}$  colloidal silicon (SYTON™) to remove any surface damage caused by mechanical polishing. The samples were given a very thin carbon coat in order to minimise charging effects and yet maintain a strong crystallographic signal (Prior et al., 1996).

### 3.2. Orientation contrast imaging

Forescatter orientation contrast (OC) images are generated by detectors in a scanning electron microscope positioned in front of samples. These are grey scale images in which grey scale variation is related to misorientation of the crystal lattice of individual grains. Where grains have not been deformed they will appear homogeneous in OC images. If, however, deformation has occurred then the grain will contain variation in grey scale as a result of misorientation of the lattice, though the images are qualitative and so the level of grey scale variation does not relate to the amount of misorientation which has occurred but does allow areas of potential interest to be located relatively rapidly for EBSD analysis (for further details see Prior et al., 1996, 1999).

### 3.3. EBSD

All pyrite crystallographic orientation data were collected by EBSD at Liverpool University using a Philips XL30 SEM with a tungsten gun and a CamScan X500 crystal probe SEM with a thermionic field emission gun. In both SEMs, the polished specimen surface was at  $20^\circ$  to the incident beam. An accelerating voltage of 20 kV with a typical beam current of

$\sim 5\ \text{nA}$  was used. Electron backscatter patterns were collected on a phosphor screen and processed using the software package CHANNEL 5 (HKL Technologies Ltd., Denmark). The angular resolution of this technique is typically better than  $1^\circ$  for both SEMs. Spatial resolution is about  $0.5\ \mu\text{m}$  on the Philips XL30 and  $0.05\ \mu\text{m}$  on the CamScan X500 (Ohfujii et al., 2005). All of the EBSD data were collected via automatic mapping using the FASTRACK stage to collect on rectangular grids with  $5\ \mu\text{m}$  spacing (Prior et al., 2002). Maps with  $0.1\ \mu\text{m}$  spacing were constructed for selected areas of each sample in order to determine finer grained textures at pyrite grain boundaries.

### 3.4. EBSD data processing

EBSD data have been post processed using the Tango utility within CHANNEL 5 software. All of the samples were processed in a systematic way in order to remove the maximum amount of non-indexed points while retaining a data set of accurate results (for further details of the processing routine used see Bestmann and Prior, 2003). The average number of points initially indexed within each sample was between 50 and 60% and using this reconstruction method, map coverage improved to as much as 90%.

Pyrite also generates EBSPs which due to pseudosymmetry can be difficult to index correctly and result in these points becoming erroneously rotated  $90^\circ$  about  $\langle 100 \rangle$  from the actual result. On average this misindexing is very minor and in the processed maps generally accounts for less than 5% of data points. These can be systematically removed using the Tango utility and will generally result in correct rotation of at least 95% of misindexed results.

Further processing was undertaken to produce data sets for pole-figure plotting in which there is just one point for each grain: a grain defined as having  $>5^\circ$  misorientation with its touching neighbours and being greater than  $10\ \mu\text{m}$ . The processed data are plotted as pole figures in the reference frame ( $XYZ$ ) (Fig. 3) defined from the shortening plane ( $XY$  plane) and the shortening direction ( $Y$ ). The pole figures are oriented with  $XY$  in the drawing plane,  $Z$  normal to the drawing plane and  $X$  vertical, as in Fig. 7Ai, ii, iii. All pole figures were plotted using the PFch5.exe program published by David Mainprice ([ftp://saphir.dstu.univ-montp2.fr/pub/TPHY/david/CareWare\\_Unicef\\_programs/PC](ftp://saphir.dstu.univ-montp2.fr/pub/TPHY/david/CareWare_Unicef_programs/PC)). Misorientation angle distribution plots were also generated to determine the relationships between correlated and uncorrelated grains within each individual sample (for further details on these plots see Wheeler et al., 2001).

A measure of crystallographic preferred orientation (CPO) was calculated using PFch5.exe, to generate the pole figure J (pfJ) index. The pfJ index uses the formulation of Michibayashi and Mainprice (2004); a random distribution is characterized by a pfJ index of unity whereas a single crystal will have a much larger pfJ index. It has been most widely used in geology for characterisation of olivine rocks where there is an effective upper value limit for pfJ of about 60 (Michibayashi and Mainprice, 2004).

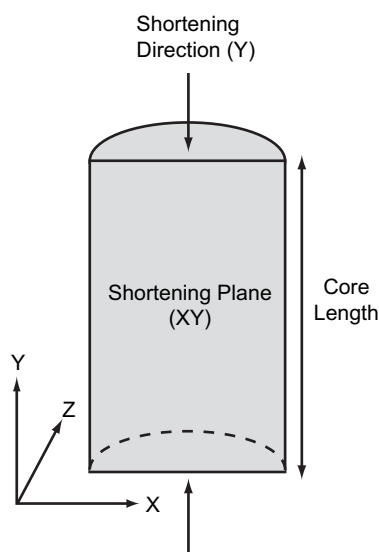


Fig. 3. Schematic illustration of the reference orientations  $XYZ$  relative to the sample cores.

### 3.5. Microprobe analysis

Qualitative analysis was carried out using an Oxford Instruments ISIS system attachment to the Philips XL30 SEM in order to identify the minor phases. An accelerating voltage of 20 kV was used, with a beam current of 3 nA, a working distance of 12 mm with approximate detection limits of about 0.1–0.5 wt%. Elements analysed were; sulphur (S), iron (Fe), copper (Cu), zinc (Zn), lead (Pb), silver (Ag), arsenic (As), barium (Ba), oxygen (O), gold (Au) and titanium (Ti).

### 3.6. Grain size, shape, distribution and orientation

The Tango utility within Channel+v5, calculates grain size, aspect ratio, long axis orientation and centre co-ordinates. These data have been used to determine grain shape and grain-shape orientation as well as calculate crystal-size distributions using CSDcorrections 1.36 software (Higgins, 2000, 2002). The mean aspect ratio and orientation of pyrite grains was calculated by plotting data from the Tango utility using Ellipstat software. This calculated the average strain ellipse for each sample and produced an Elliot plot with mean  $R_f$  (aspect ratio) and  $\phi$  (long axis orientation) values and potential errors (Table 2).

Crystal size distribution (CSD) calculations use corrections made for the intersection probability effect and partial corrections for the cut-section effect. The approximate particle shape and rock fabric must be known to make these corrections. For this study all pyrite grains were treated as ellipses in 2D sections, and the long axis dimension of each grain was used in CSD calculations. Grain shape corrections were made on the basis of measured ellipse ratios in section (Higgins, 2002).

## 4. Results

### 4.1. Sample B-1 (starting material)

Sample B-1 is a core of the pyrite ore starting material (Cox et al., 1981) and so serves as a control to identify changes in the experimentally deformed samples. There are two types of layering present parallel to the coring direction within the

sample: a grain-size layering defined by 40–80  $\mu\text{m}$  pyrite grains and smaller 20–40  $\mu\text{m}$  grains and also a compositional layering defined by the minor phases. Pyrite grain sizes measured in 2-D sections average about 38  $\mu\text{m}$  (Fig. 4A) and range up to 200  $\mu\text{m}$  in size. The CSD is straight with an initial curve at fine grain sizes and suggests the majority of pyrite grains are 100  $\mu\text{m}$  or smaller (Fig. 4B and C). There is a suggestion of a weak grain elongation in the direction of layering, but it appears to be biased to the largest pyrite grains. Pyrite grain orientations suggest a weak SPO (Fig. 5A) with an orientation similar to layering direction and an average aspect ratio of about 1.2 (Table 2). Pyrite grains are predominantly idiomorphic in shape with rounded edges and boundaries between grains are generally quite straight or gently curved and in places display apparent ‘foam’ textures (Fig. 7A). There are very few inter- or intra-granular fractures within the sample.











The OC images of the pyrite grains show little or no variation in grey scale within grains. EBSD was used to construct eight Euler-angle maps across the area of sample covering a total area of about 8 mm<sup>2</sup>. There is little evidence for lattice misorientation within grains, with a maximum intra-grain orientation spread for 95% of the grains of 2° although generally less (Fig. 6). Where lattice rotation has occurred it is either about a single  $\langle 100 \rangle$  axis (Fig. 7Bi) or more rarely about a single  $\langle 110 \rangle$  axis (Fig. 7Biv). Low angle misorientation boundaries (Fig. 7D) within pyrite grains are sparse with only a few pyrite grains within each mapped area containing any at all. The neighbour-pair misorientation histogram has a low angle peak (2°) which is three and a half times lower than the theoretical random distribution peak at about 60° and is not far from a theoretical random distribution (Fig. 7E). The random-pair histogram closely follows the theoretically random distribution. Pole figures for 1 point per all pyrite grains measured show a uniform (random) distribution of points which is mirrored by the low pfJ factor of 1.02 (Fig. 7F).

### 4.2. Run 048 (34% shortening at 550 °C and strain rate of $2 \times 10^{-4} \text{ s}^{-1}$ )

This sample is the lowest temperature experimental run (Cox et al., 1981). Pyrite grain sizes measured in 2-D sections

Table 2

Summary table listing temperature, mean grain size and the measured and theoretical strain ellipses for pyrite grains in all of the samples

Sample	B-1 (XY)	048	092	059	053
Temperature (°C)	–	550	600	650	700
Experimental shortening (%)	–	34	22	40	32
Mean grain size ( $\mu\text{m}$ )	38	33	45	34	38
Measured grain shape and orientation					
Aspect ratio ( $R_f$ )	1.2 $\pm$ 0.02	1.01 $\pm$ NAN	1.08 $\pm$ 0.02	1.07 $\pm$ 0.01	1.05 $\pm$ 0.01
Orientation of X axis ( $\phi$ )	90.4 $\pm$ 3.1	87.8 $\pm$ NAN	55 $\pm$ 8.4	15.8 $\pm$ 4.6	50 $\pm$ 7.7
Strain shape change shortening (%)	–	34	19.4	54	28
Expected theoretical grain shape					
Aspect ratio	1.2	1.02	1.06	1.006	1.022

The mean shape orientation for all samples has 90° as the Y direction or the length of the cylinder, mean deviation is given for all samples, except 048 where the ellipse passes through the origin and thus results in no figure or NAN (not a number). Shape change shortening is the amount of shortening in each sample which can be accounted for by shape change of pyrite grains.



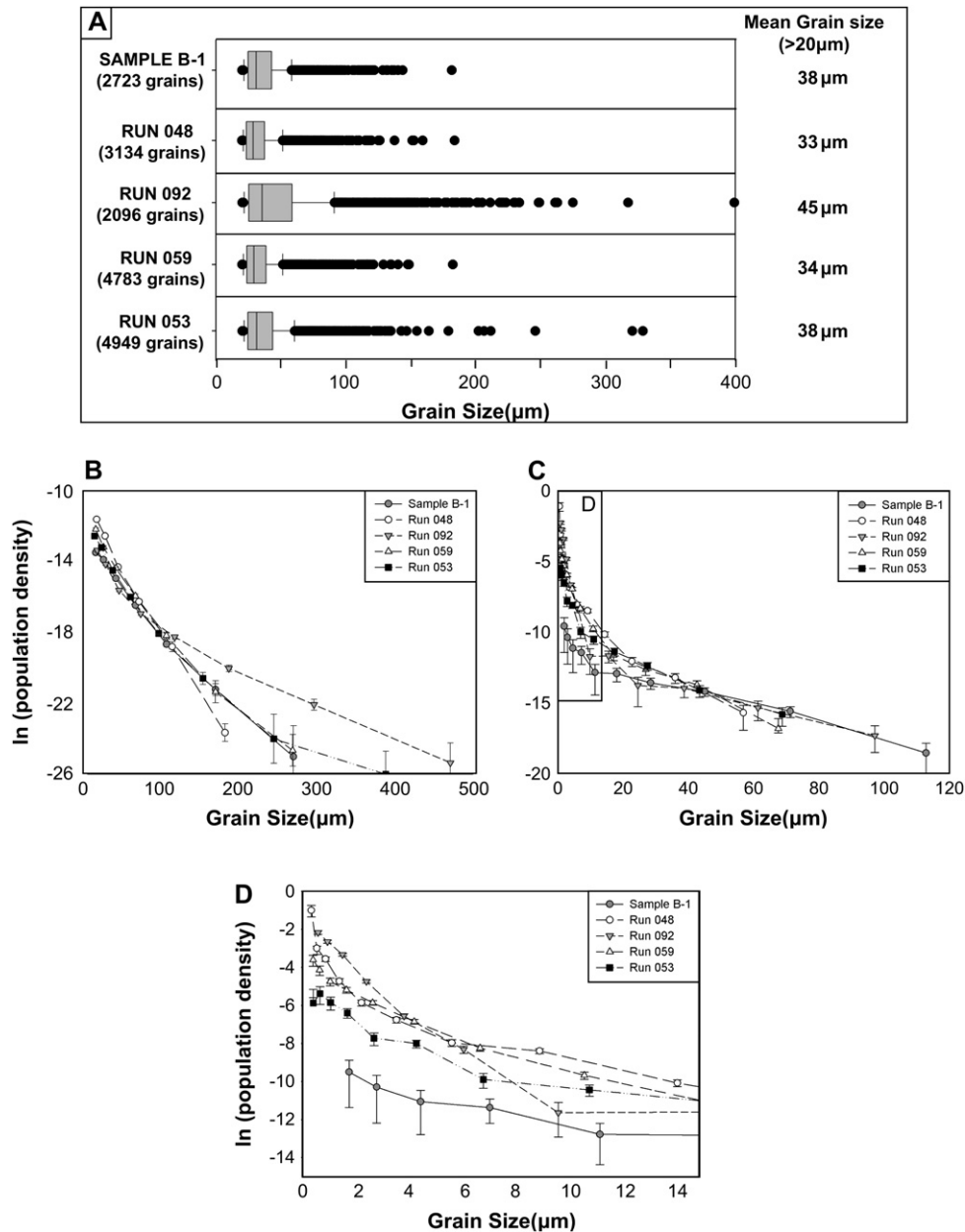


Fig. 4. (A) Box plots of grain size for all samples, with all grains smaller than  $20\ \mu\text{m}$  removed: boxes represent 50% of the total data 'the body', limits of which are the interquartile range, the line within boxes is the median point of the data and the 'whiskers' represent the extremes of the data ( $3/2s$  of the interquartile range), dots out with the whiskers represent outliers and are extreme cases of the grain size variable. (B) Crystal size distribution (CSD) plot showing the population density versus grain size ( $>20\ \mu\text{m}$ ) for all of the samples. (C) Crystal size distribution (CSD) plot showing the population density versus grain size for pyrite grains down to  $0.25\ \mu\text{m}$  in all of the samples. (D) Crystal size distribution (CSD) plot showing the population density versus grain size for pyrite grains between  $0.25$  and  $15\ \mu\text{m}$  in size.

average about  $33\ \mu\text{m}$  (Fig. 4A) and range up to as much as  $200\ \mu\text{m}$  though these are rare. Pyrite boundaries with the surrounding phases often appear embayed in places and many are surrounded by a suite of fine grained ( $<10\ \mu\text{m}$ ) rounded pyrite grains. The CSD (Fig. 4C and D) is initially steep and curved suggesting a high proportion of small ( $<10\ \mu\text{m}$ ) pyrite grains. There is no prevalent SPO in the sample and the overall distribution of grain shape orientation is approximately uniform (Fig. 5B). The few grains that show elongation are generally concentrated within the area of apparent foliation. However,

aspect ratios of pyrite grains are close to circular, averaging  $\sim 1.01$  (Table 2). In reflected light grains appear homogeneous with few intra-granular fractures present (Fig. 8A).

Most of the pyrite grains show internal grey-scale variation in OC images (Fig. 8B) with a variety of patterns: straight and curved bands, checkerboard style arrays or complex. Eleven Euler angle EBSD maps were constructed across different areas of the sample covering a total area of about  $7\ \text{mm}^2$ . Pyrite grains with curved and straight bands in OC images preserve evidence of a single rotation about  $\langle 100 \rangle$  (Fig. 8Bii, iii)

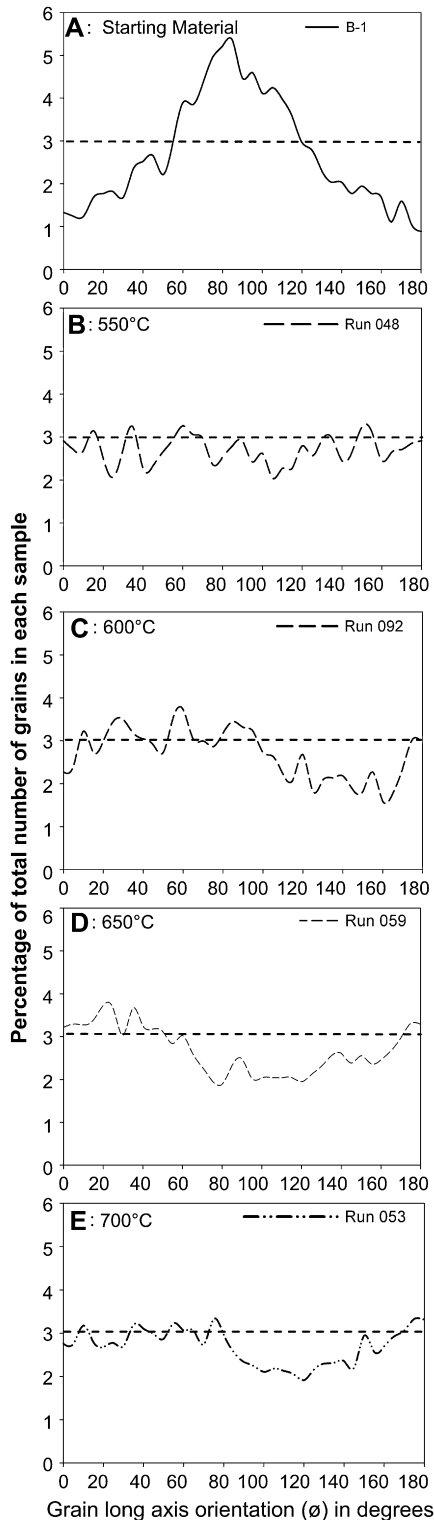


Fig. 5. Frequency histograms plotting the long axis orientation ( $\phi$ ) of all pyrite grains greater than  $20\ \mu\text{m}$  within each sample against the total percentage of grains,  $90^\circ$  orientation representing the length of the cores. The dashed line on each histogram represents 3% of the total number of grains.

while checkerboard texture preserves evidence of rotation about two separate  $\langle 100 \rangle$  axes (Fig. 8Bi and iv). Cumulative misorientation within grains is generally between about  $2$  and  $10^\circ$  (Fig. 6), but a few grains show accumulated lattice rotation

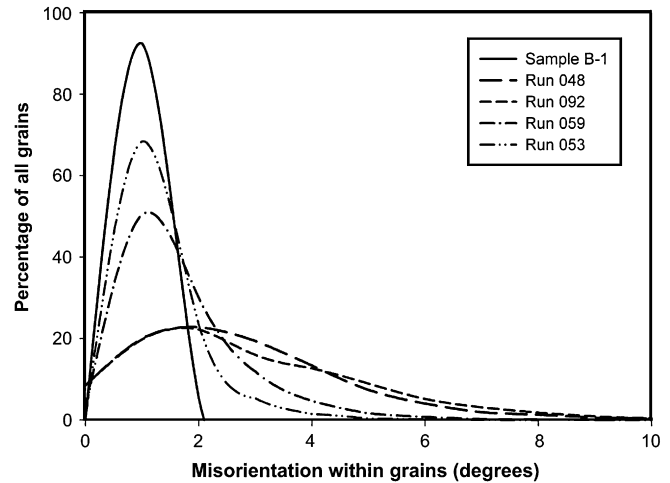


Fig. 6. Frequency histogram plotting lattice misorientation within individual grains against the total percentage of grains within each sample.

of as much as  $20^\circ$ . The sample contains numerous sub-grain boundaries (Fig. 8D), which are predominantly low-angle ( $\sim 2^\circ$ ) boundaries. The neighbour-pair misorientation angle histogram (Fig. 8E) is dominated by a low-angle ( $\sim 2^\circ$ ) boundary peak almost four times greater than the theoretical random distribution peak at  $60^\circ$ . However, the random-pair results appear to follow the theoretical random. The bulk fabric pole figures show a uniform distribution suggesting there is no overall CPO in the sample, mirrored by the low  $\sim 1.00$  pFJ factor (Fig. 8F).

#### 4.3. Run 092 (22% shortening at $600^\circ\text{C}$ and strain rate of $2 \times 10^{-4}\ \text{s}^{-1}$ )

Pyrite grain sizes measured in 2-D sections average about  $45\ \mu\text{m}$ , and range up to  $400\ \mu\text{m}$  (Fig. 4A). Reflected light observations show that some of the pyrite grains are fringed by fine ( $<10\ \mu\text{m}$ ) rounded pyrite grains. The CSD (Fig. 4C and D) is initially relatively steep with a high proportion of small grains. However, it then becomes concave upwards reflecting the greater abundance of larger grains also apparent in Fig. 5A. Ninety-five percent of the CSD-corrected pyrite grain sizes are less than  $100\ \mu\text{m}$ . Pyrite grains are equant but typically have rounded edges. A few pyrite grains are elongated (Fig. 9C, D) but there is at most a very weak SPO close to the shortening direction (Fig. 5C). The mean aspect ratio of grains is only 1.08 (Table 2). The sample is characterised by extensive randomly orientated inter- and intra-crystalline fractures.

OC images show abundant variation in grey scale within pyrite grains, principally via straight and curved bands running through grains, but also with complex and checkerboard textures. Eight Euler angle EBSD maps across the area of the sample were constructed, covering a total area of about  $8\ \text{mm}^2$ . The maps show variation in crystallographic orientation (e.g. Fig. 9B) predominantly about a single  $\langle 100 \rangle$  axis (Fig. 9Bi and ii). Lattice orientation spread about two  $\langle 100 \rangle$  (Fig. 9Biv) axes and a single  $\langle 110 \rangle$  axis (Fig. 9Biii) were

## Sample B-1 (Starting Material)

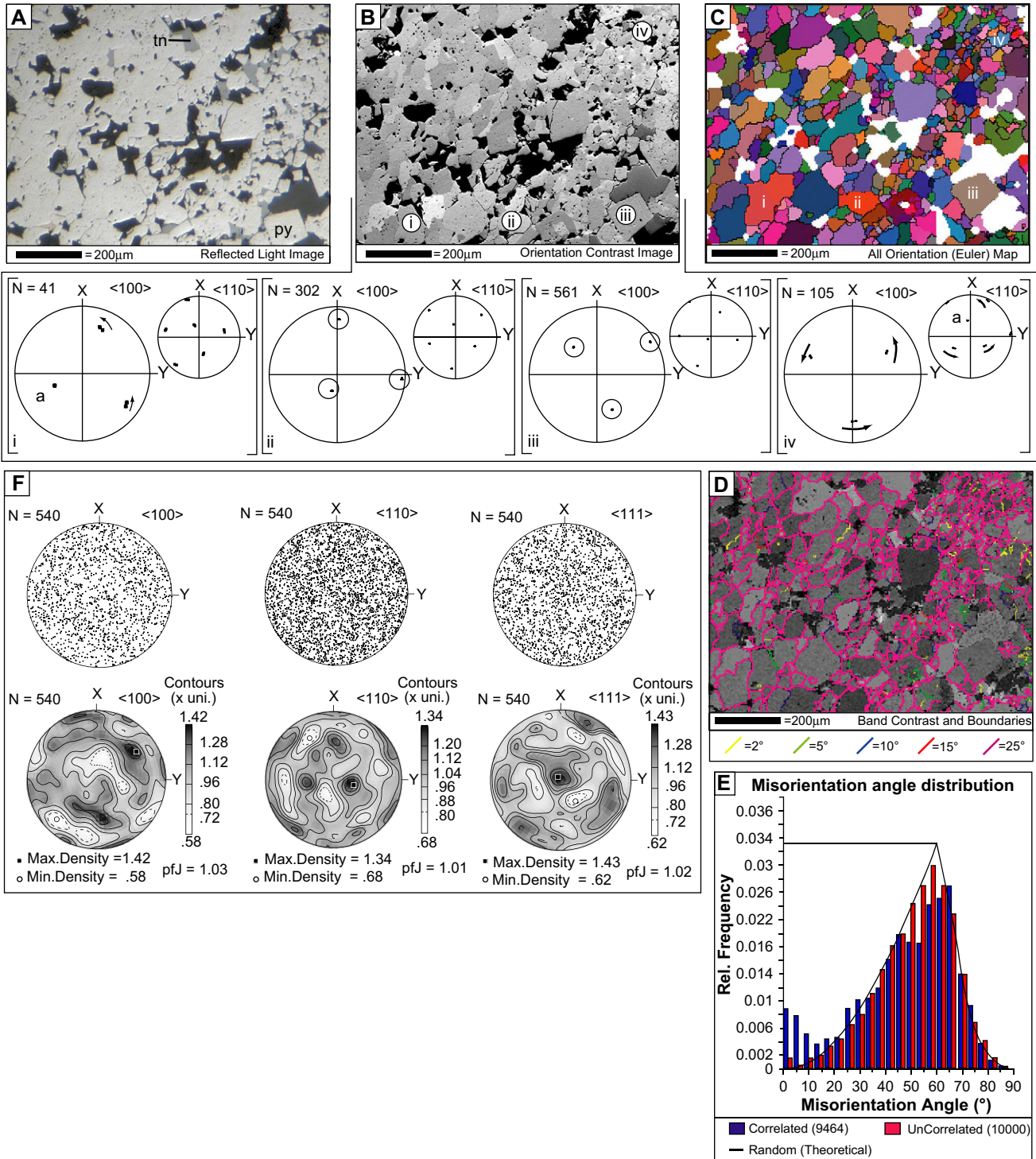


Fig. 7. (Sample B-1 (Starting material)). (A) Plane-polarised reflected-light image of the mapped areas. (B) Orientation contrast image with pole figures for selected pyrite grains, rotation direction is given by arrows and the rotation axis by a and or b, pole figures showing no rotation are circled. (C) EBSD map showing all Euler angles with selected pole figure grains marked on, subtle variation in colour represents a change in crystallographic orientation. (D) EBSD map showing the band contrast image overlain by misorientation boundaries. (E) Misorientation angle distribution for pyrite grains in mapped area. (F) Pole figure plots for 1 point per grain for the entire map shown, all plots shown are in the upper hemisphere.

also observed in a few grains. The sample has abundant low angle ( $\sim 2^\circ$ ) sub-grain boundaries within pyrite grains (Fig. 9D). These dominate the neighbour-pair misorientation-angle histogram (Fig. 9E), whereas the random-pair

results appear to follow the theoretical random distribution. The low angle ( $2^\circ$ ) neighbour-pair peak is almost four times greater than the theoretical random  $60^\circ$  peak (Fig. 9E). Pole figures for all pyrite grains measured indicate there is no



Run 048 (550°C)

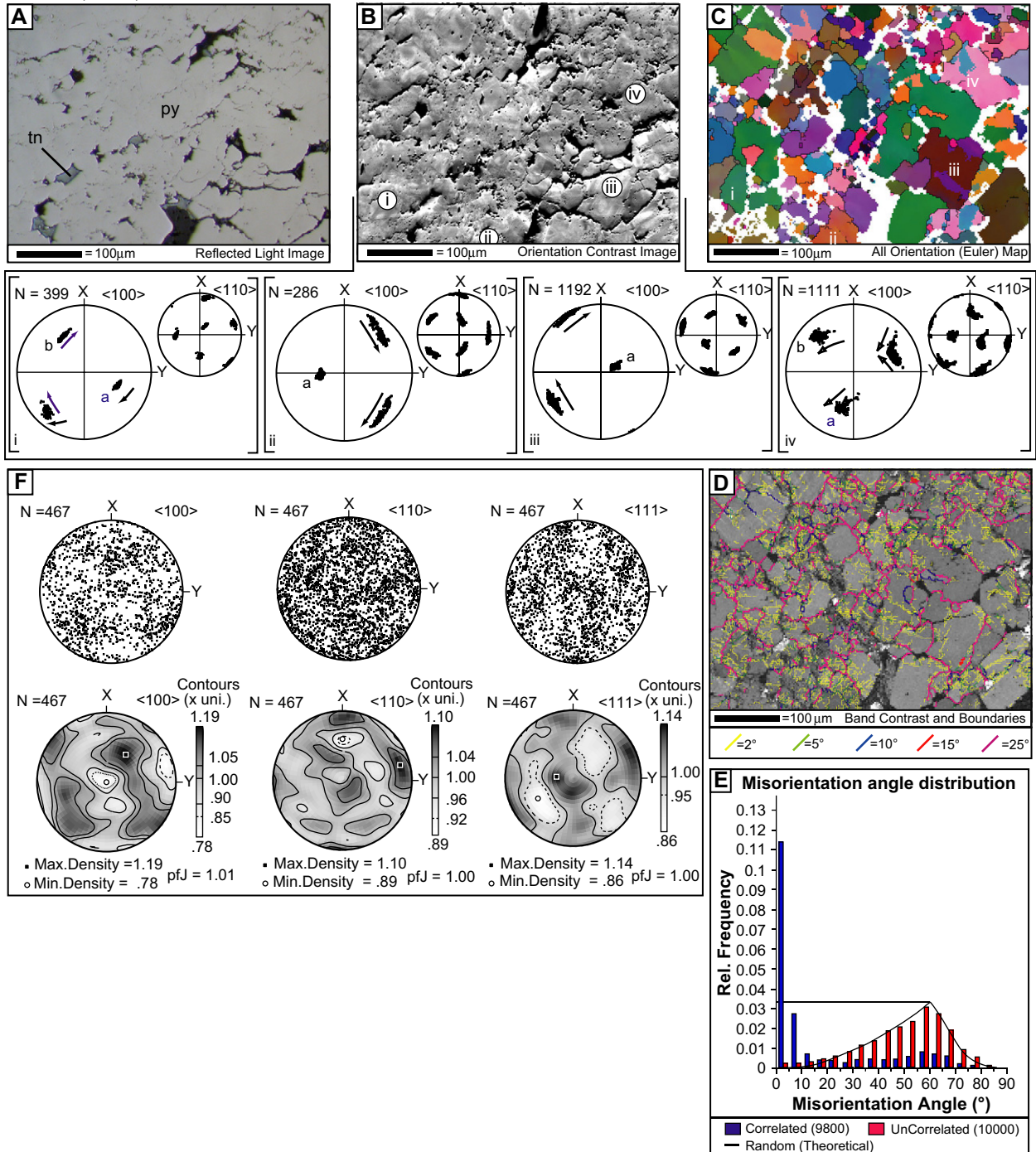


Fig. 8. (Run 048 (550 °C)). See caption for Fig. 7.

sample-scale CPO of pyrite grains and the distribution is uniform (random) as reflected in the low Pfj factor  $\sim 1.02$  (Fig. 9F).

4.4. Run 059 (40% shortening at 650 °C and strain rate of  $2 \times 10^{-4} s^{-1}$ )

Pyrite grain sizes measured in 2-D sections average about 34  $\mu m$  (Fig. 4A) and range up to about 200  $\mu m$ . In reflected

light there is an obvious suite of smaller pyrite grains surrounding many of the larger pyrite grains. The CSD (Fig. 4C and D) shows an abundance of grains smaller than 20  $\mu m$  before becoming much shallower at larger grain sizes (Fig. 4B). Almost all pyrite grains are less than 100  $\mu m$  in diameter. Grains typically have rounded edges and the boundaries between pyrite grains are very unclear, with some appearing very irregular and many appear significantly embayed. Pyrite grain orientations calculated in Tango



Run 092 (600 °C)

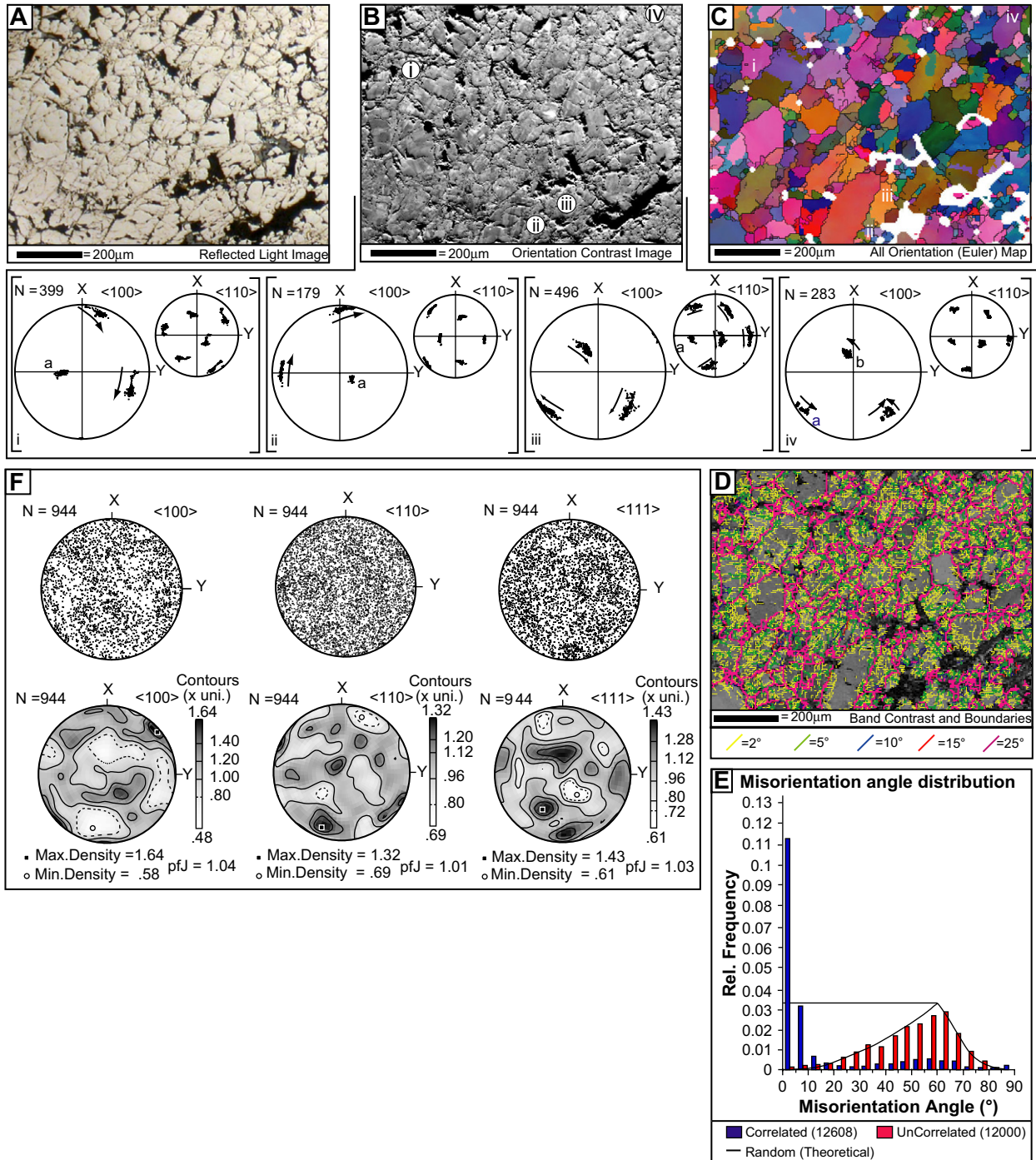


Fig. 9. (Run 092 (600 °C)). See caption for Fig. 7.

(Fig. 5D) and processed in Ellipstat suggest that there is no SPO and pyrite grains have an average aspect ratio of 1.072 (Table 2). The sample contains few if any inter- or intra-crystalline fractures.

OC Images (Fig. 10B) show pyrite grains with obvious variation in grey-scale, but also apparently homogeneous grains. Eight Euler angle EBSD maps across the area of the sample were generated covering a total area of about 8 mm<sup>2</sup>. The grains with OC image grey-scale variation (Fig. 10B) show

lattice orientation spread primarily about a single <100> axis (Fig. 10Bii), typically by <5° with some recording misorientations up to 10° (Fig. 6). However, some also show orientation spread about two separate <100> axis (Fig. 10Biv) as well as a single <110> (Fig. 10Bi). Pyrite grains contain a few low-angle (2°) sub-grain boundaries (Fig. 10D). The neighbour-pair misorientation-angle histogram (Fig. 10E) has a low-angle (2°) boundary peak double that of the random theoretical 60° peak. However, the random-pair results follow the theoretically

Run 059 (650 °C)

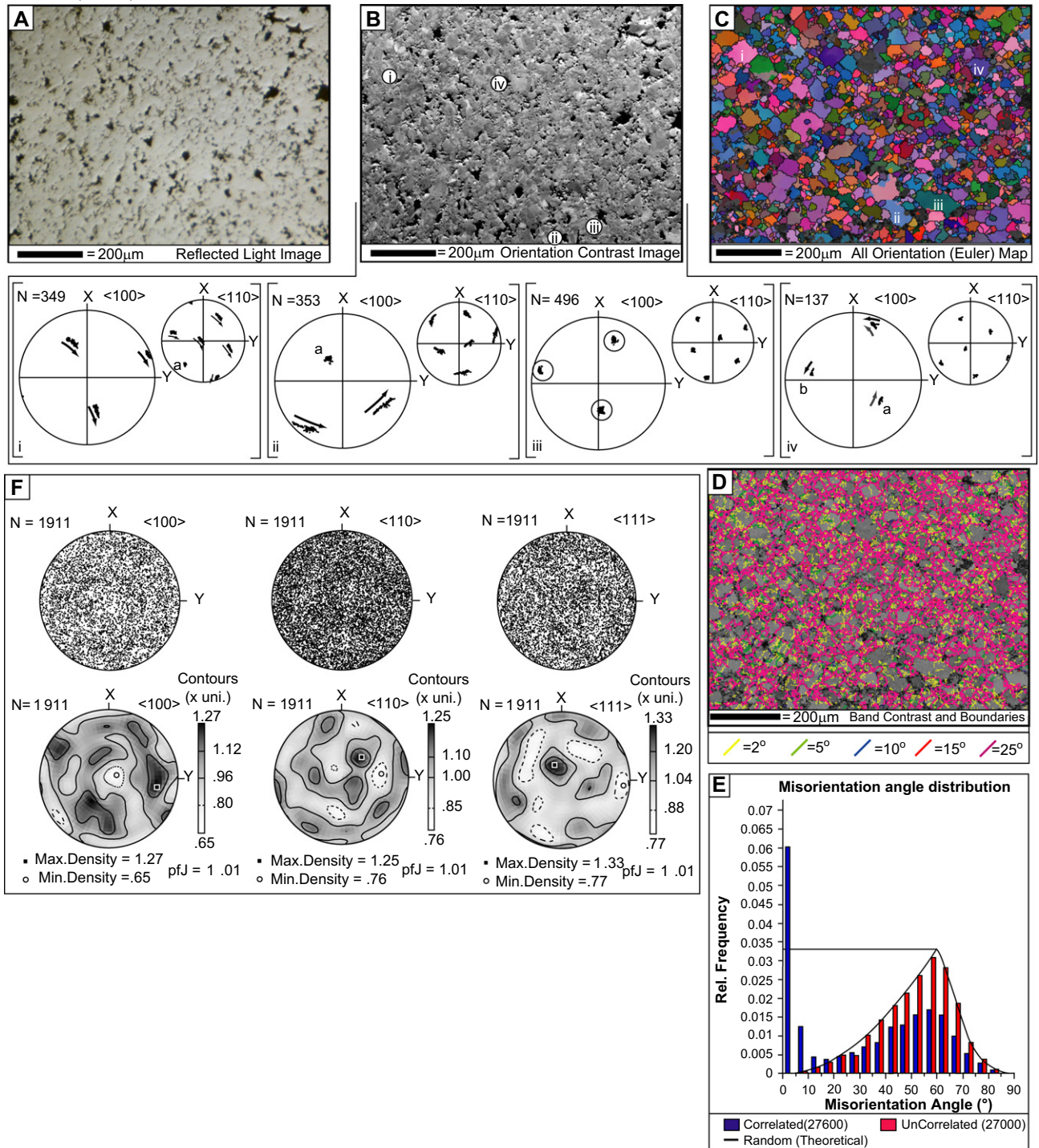


Fig. 10. (Run 059 (650 °C)). See caption for Fig. 7.

random distribution. The pyrite grains in this sample have a uniform bulk CPO reflected in the low Pf<sub>J</sub> of ~1.01 (Fig. 10F).

4.5. Run 053 (32% shortening at 700 °C and strain rate of  $2 \times 10^{-4} \text{ s}^{-1}$ )

This sample is the highest temperature experimental run (Cox et al., 1981). Pyrite grain sizes measured in 2-D sections

average about 38 μm but can range up to 300–350 μm (Fig. 4A). The CSD is initially linear (Fig. 4C and D) but with increasing grain size it curves upward (Fig. 4A) reflecting the presence of a number of large grains. A few of the largest pyrite grains are equant in shape but the majority have rounded edges with most boundaries between pyrite grains appearing irregular and locally embayed. Grains have an average aspect ratio of ~1.01 (close to circular) with no SPO (Table 2; Fig. 5E).



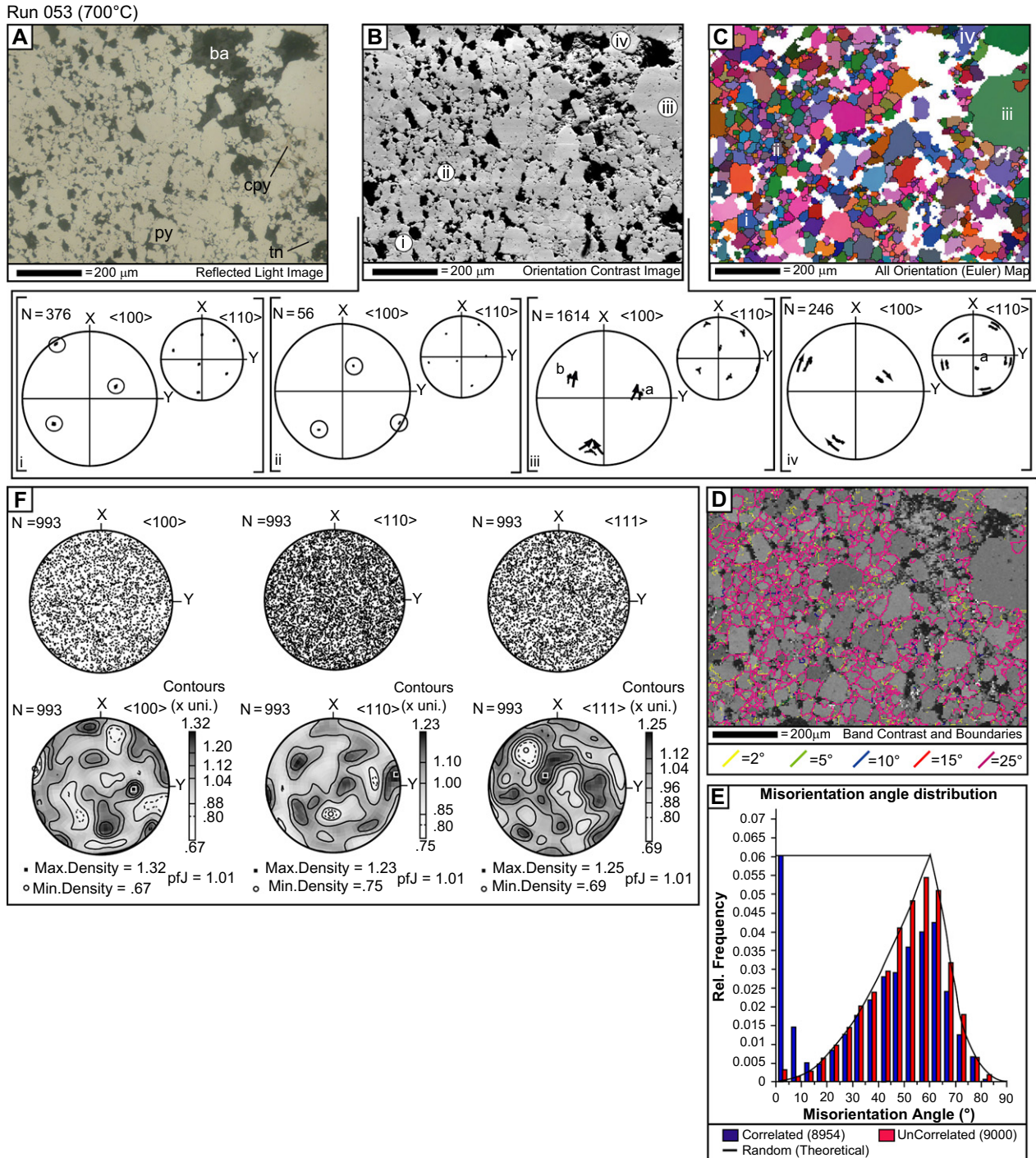


Fig. 11. (Run 053 (700 °C)). See caption for Fig. 7.

OC images (e.g. Fig. 11B) suggest little or no grey-scale variation within pyrite grains. Ten Euler-angle EBSD maps across the area of the sample were generated covering a total area of about 10 mm<sup>2</sup>. The grains which do show OC variation also show lattice orientation spread (Fig. 11B), about two separate  $\langle 100 \rangle$  axes (Fig. 11Biii) and also about a single  $\langle 110 \rangle$  axis (Fig. 11Biv) up to a maximum of 6°. However the majority of pyrite grains show little or no orientation spread (Fig. 6). There are low-angle ( $\sim 2^\circ$ ) sub-grain boundaries present within grains but these are generally restricted near to grain

boundaries (Fig. 11D). The neighbour-pair misorientation angle histogram has a low angle ( $2^\circ$ ) peak which is equal in height to the random theoretical  $60^\circ$  peak (Fig. 11E). Random pair results have a theoretically random distribution. The results suggest that pyrite grains have a uniform CPO (Fig. 11F).

#### 4.6. Minor phases

An understanding of the behaviour of the minor phases (tennantite, barite, chalcopyrite) during deformation with

respect to the pyrite is important in understanding to an extent how the various micro-structures in the pyrite may have evolved within the samples as a whole.

The principal minor phase in the samples is tennantite (Table 1) and in reflected light is light grey-bluish. Chalcopyrite appears as a dull yellow in reflected light and is less common in the samples; occurring as interstitial grains in the starting material (B-1) and the low temperature runs (048 and 092) and as discrete vein like features parallel to the shortening direction in the higher temperature runs (059 and 053). The least abundant minor phase is barite, which is dark grey in reflected light (Table 1). All of these phases microhardness is much lower than pyrite and this has resulted in a poorer polish for these phases. In OC images they often appear as a lower elevation phase than the pyrite and in most of the samples they produce faint EBSPs at best, and often none at all, particularly the barite. Due to these constraints results are only presented here where indexing was possible from the tennantite in the undeformed starting material (B-1) and the lowest and highest temperature deformed runs (048 and 053).

#### 4.6.1. Sample B-1 (tennantite)

The tennantite in the starting material appears homogeneous in reflected light and in places appears to form layers in the ore. The OC images generated show little and generally no variation in grey scale (Fig. 12A). Six Euler angle EBSD maps at a spatial resolution of  $0.1\ \mu\text{m}$  were constructed across the area of the sample where EBSPs would index. All of the maps generated suggest that the tennantite areas between pyrite grains generally contain just one or two large equant grains. Euler angle maps show little or no variation in colour (Fig. 12B) and there are only one or two low angle ( $\sim 2^\circ$ ) boundaries present and generally none at all. The pole figures show no lattice rotation (Fig. 12C).

#### 4.6.2. Run 048 $550^\circ\text{C}$ (tennantite)

The OC images of tennantite in the lowest temperature run show little if any variation in grey-scale (Fig. 13B). Eight Euler angle EBSD maps at a spatial resolution of between  $0.1$  and  $0.5\ \mu\text{m}$  were constructed across the area of the sample. The Euler angle and grain boundary maps (Fig. 13C and F) indicate modification of the tennantite grain size. A few elongate large tennantite grains about  $20\text{--}30\ \mu\text{m}$  in diameter are

surrounded by clusters of much smaller ( $<10\ \mu\text{m}$ ) rounded grains of tennantite. The large tennantite grains contain evidence in pole figures for lattice rotation about both a  $\langle 111 \rangle$  and a  $\langle 110 \rangle$  direction with accumulative misorientation of as much as  $10^\circ$  (Fig. 13D, E). The smaller rounded grains, however, show little or no evidence for internal lattice misorientation (Fig. 13G).

#### 4.6.3. Run 053 $700^\circ\text{C}$ (tennantite)

The highest temperature runs contains chalcopyrite as vein like features within the core of the sample and tennantite tends to form thin films around pyrite grains. Five Euler angle EBSD maps at a spatial resolution of  $0.1\ \mu\text{m}$  were constructed across the sample. In OC images (Fig. 14A) the tennantite shows little obvious grey scale variation, although the surface is much more pitted and irregular than in the previous samples (B-1 and run 048). The Euler angle maps show tennantite grains are elongated and can be as much as  $50\ \mu\text{m}$  in length (Fig. 14B). There are numerous low angle ( $2^\circ$ ) boundaries within tennantite grains and misorientation plots across individual grains shows accumulated orientation spread of as much as  $7^\circ$  (Fig. 14C).

## 5. Discussion

The results presented so far address a number of questions about how micro-structural development within pyrite grains changes with temperature:

- What processes facilitate these textural changes?
- How does grain size, shape and shape orientation change?
- What processes accommodate shortening?
- How does intra-grain and whole sample crystal orientation change?

### 5.1. Grain size, shape and orientation

The box plots in Fig. 4A suggest that there is very little mean grain size variation between B-1 and the deformed samples, yet subtle trends are identified from CSD data (Fig. 4). Even at grain sizes above  $20\ \mu\text{m}$ , runs 048, 059 and 053 all have steeper CSD slopes than the starting material B-1

Sample B-1 - Tennantite (Experimentally undeformed)

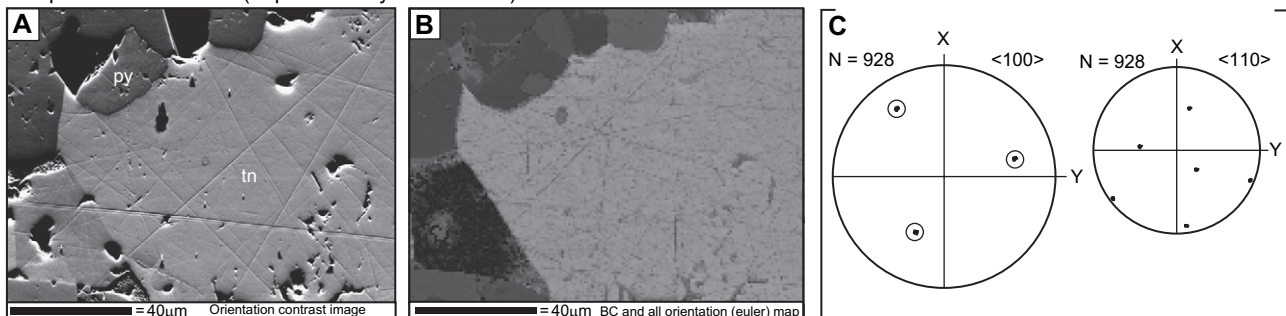


Fig. 12. (A) Orientation contrast image of tennantite. (B) Orientation map of tennantite. (C) Pole figure of the large grain shown.



Run 048 - Tennantite (550°C)

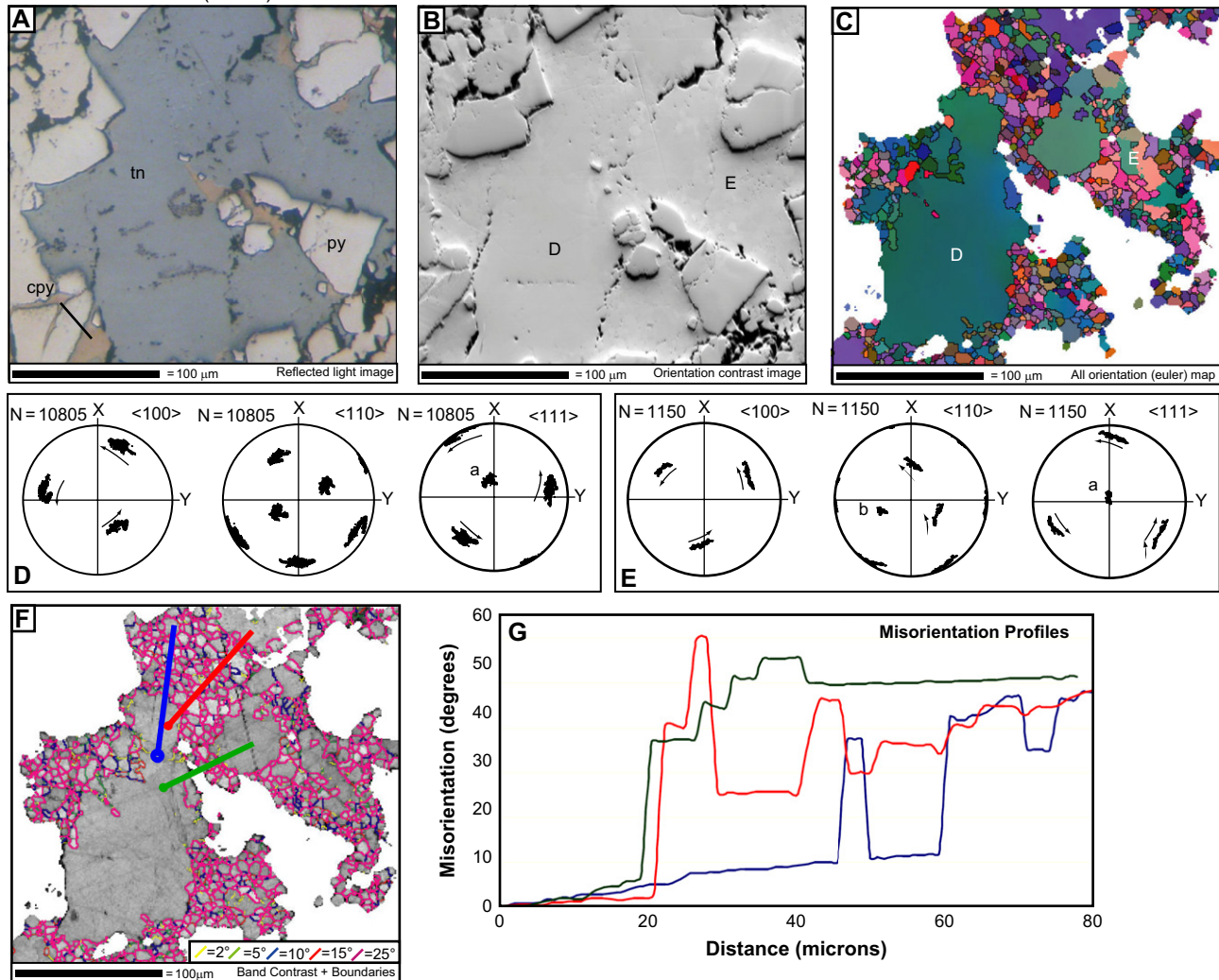


Fig. 13. (A) Reflected light image of the mapped area showing chalcopyrite (cpy), tennantite (tn) and pyrite (py). (B) Orientation contrast image of tennantite showing the distinct change in relief between pyrite and tennantite grains. (C) Orientation map of tennantite. Crystallographic orientation variations are represented by different colours assigned in Euler space. Pole figures for grains (D) and (E) are shown. (F) Band contrast image with overlain boundaries. (G) Misorientation profiles relative to first point crossing both 'core' and 'mantle' grains as indicated in (C).

(Fig. 4B). The concave-up CSD for run 092 (Fig. 4B) reflects an increase in the number of larger pyrite crystals, consistent with the tail of outliers in Fig. 4A. While this may reflect some process of grain size increase during the deformation experiment, it is perhaps more likely that the grain size of the original core for run 092 differed significantly from sample B-1, sampling a coarser domain within the Blow ore block. All of the deformed samples clearly have a much larger proportion of small (20  $\mu\text{m}$ ) pyrite grains than the initial starting material (Fig. 4C, D). This would be consistent with grain size reduction and the development of new grains during the deformation experiments. As deformation and temperature of the samples increase from 550 °C to 700 °C the slope of the small grain size fractions becomes shallower. These results suggest that two possible scenarios have occurred. Either increasing temperature has resulted in a change in the recrystallisation mechanisms operating, whereby in the lower

temperature runs recrystallisation mechanisms generate lots of new small pyrite grains and at high temperatures this changes to a mechanism where fewer new small pyrite grains are generated and so shallower CSD slopes are produced. The other possibility is that the same mechanism of recrystallisation is operating at all temperatures, but at lower temperatures it is more important.

Variation in grain shape aspect ratio ( $R_f$ ) and long axis orientation ( $\phi$ ) of pyrite grains is apparent in all of the deformed runs when compared with the initial starting material (B-1). The initial starting shapes of grains in the XY plane have an  $R_f$  of about 1.2 (Table 2). All of the deformed runs have a lower  $R_f$  than this reflecting a shape change. In order to determine how much shape change has occurred relative to the shortening applied, the theoretical grain shape change for each sample was calculated, assuming that the initial starting grain shape in all of the runs is equivalent to that measured in B-1 and that

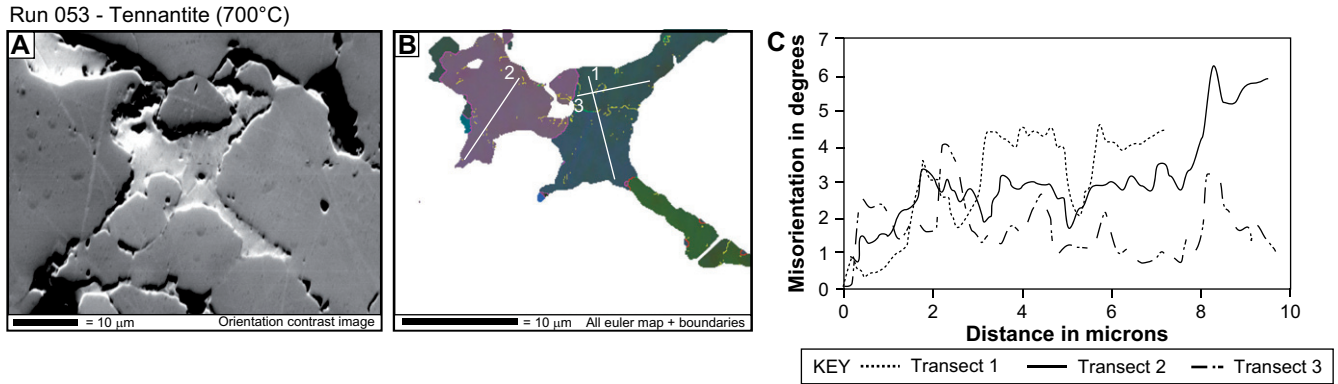


Fig. 14. (A) Orientation contrast image of tennantite grains. (B) Orientation map with grain and sub-grain boundaries overlain. (C) Misorientation profiles across selected grains.

experimental shortening was homogeneous and occurred via pure shear.

Measured grain shapes ( $R_f$ ) are comparable to the calculated ones in 048, 092 and 053 (Table 2) suggesting that most if not all of the shortening in these samples could have been taken up through change in pyrite grain shape. The  $R_f$  values suggest that in all cases the grain shapes in the deformed runs have changed from essentially prolate grains in B-1 to spheres. This will account for the lack of shape preferred orientation (SPO) as low aspect ratio grains cannot produce a strong SPO. The shape and orientation of the grains in Run 059 suggests that slightly more shortening has been recorded by this sample. One possibility is that the strain has been partitioned heterogeneously throughout the core, and that the particular section analysed in this study has experienced more shortening. It is also possible that the starting grain shape in 059 was different to B-1.

### 5.2. Textural changes and accommodation mechanisms

Determining which deformation and recovery mechanisms are active (Table 3) within the samples as a whole is essential in understanding how and possibly why the micro-structures

present have evolved. The presence of numerous low-angle ( $2^\circ$ ) sub-grain boundaries within pyrite grains coupled with cumulative rotation within pyrite grains suggests a plastic deformation mechanism in the lowest temperature runs (048 and 092). The formation of sub-grain boundaries or dislocation walls (Cox, 1987) requires both dislocation glide and climb to occur and thus the active deformation mechanism in 048 and 092 was dislocation creep coupled to recovery, which has led to an obvious change in shape of pyrite grains (Table 2) but not the development of any bulk pyrite crystallographic preferred orientation (CPO). While dislocation creep and associated shape change appears to account for most of the shortening in runs 048 and 092 other mechanisms are also clearly active.

There is an obvious suite of smaller ( $<10 \mu\text{m}$ ) rounded pyrite grains surrounding the larger pyrite grains visible in reflected light microscopy, which is also apparent in the CSD plots (Fig. 4). The texture present in run 048 of large pyrite 'porphyroclast' grains surrounded by clusters of smaller ( $<10 \mu\text{m}$ ) rounded 'recrystallised' pyrite grains is characteristic of the features of bulging recrystallisation (Table 2). The high spatial resolution band contrast and boundary maps (Fig. 15) are similar to what has been described as regime 1

Table 3

Diagnostic microstructures of the deformation and recrystallisation mechanisms which are potentially operating within the experimentally deformed samples

Mechanism	Diagnostic microstructures
Dislocation glide	Misorientation within grains, few and generally no dislocation walls formed, lattice bending, deformation bands often form
Dislocation creep	Stepped misorientation within grains due to dislocation walls forming, often results in a strongly developed crystallographic preferred orientation (CPO)
Diffusion creep	No misorientation within grains, no dislocation walls, grain boundaries are often relatively straight, pressure shadows, loss or at least weakening of any previous CPO
Super plasticity	Generally requires a fine grained aggregate material ( $1-10 \mu\text{m}$ ), grains often equi-dimensional, no shape preferred orientation (SPO) or CPO developed
Bulging recrystallisation (blg)	New small $1-5 \mu\text{m}$ recrystallised grains are formed surrounding old 'relict' grains, new grains have few if any dislocations, relict grains contain embayments equivalent to new recrystallised grains
Sub grain rotation recrystallisation (SGR)	Old 'relict' grains are flattened or ribbon shaped and contain dislocations, recrystallised grains contain few if any dislocations, new grain size is much larger than with bulging, often forms a characteristic 'core' and 'mantle' texture
Grain boundary migration recrystallisation (GBM)	Grain boundaries are generally very curved and lobate, few if any dislocations are present within grains, new grain size can be variable, difficult to distinguish old 'relict' grains from new 'recrystallised' ones

by Hirth and Tullis (1992) (Fig. 16) which appears to be the dominant recrystallisation process in run 048. Run 092, while having similar characteristics, appears to contain evidence for sub-grain rotation (SGR) processes. This is suggested by the much larger size of the recrystallised pyrite grains and their

misorientations compared with the parent grains. However, while this process may be operating there is also significant evidence for bulging and so 600 °C may represent conditions at which recrystallisation is changing from regime 1 (bulging) to regime 2 (SGR) (Fig. 16).

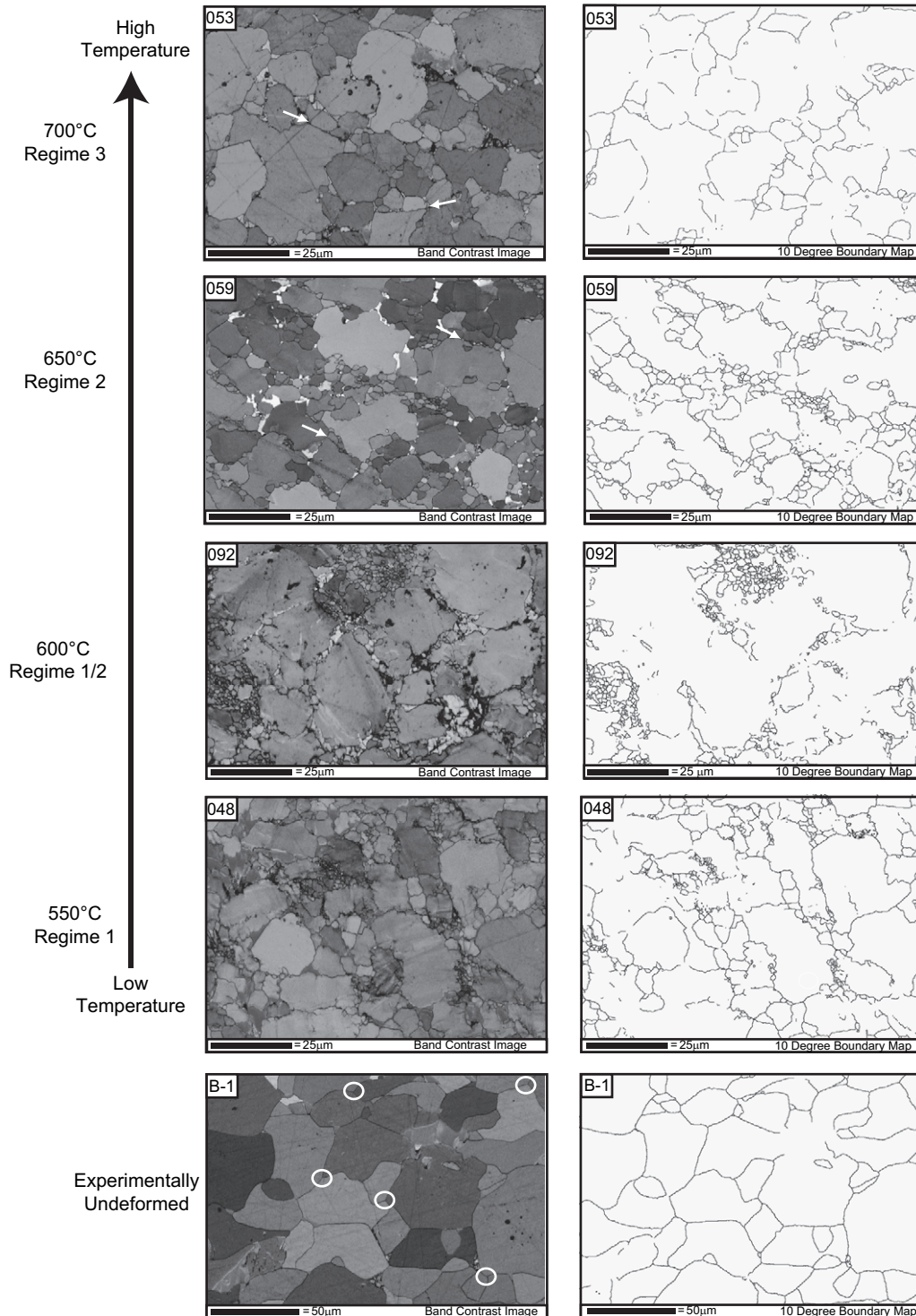


Fig. 15. High spatial resolution band contrast and boundary maps of all the samples showing boundary and grain size changes with temperature. Most of the grain boundaries in B-1 form a 'foam' texture, with a few highlighted with circles and arrows in the other images indicate potential grain boundary sliding surfaces. The boundary maps do not show all of the grain boundaries present due to the problem of non-indexing along grain boundaries and subsequent noise reduction methods failing to fill all of the gaps.



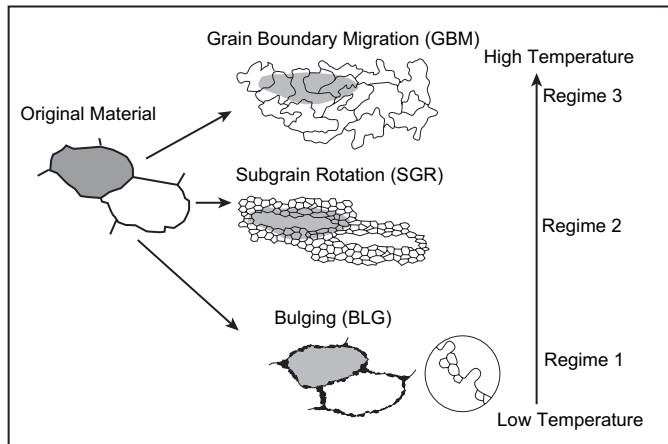


Fig. 16. (A) Schematic diagram showing the characteristic appearance of the three types of dynamic recrystallisation potentially operating in the deformed samples (adapted from Passchier and Trouw, 2005), regime 1, 2 and 3 refer to those from Hirth and Tullis (1992).

Another mechanism which is likely to be operating in the low temperature runs is grain boundary sliding. This would result in pyrite grains slipping past one another without any significant shape change of grains. Evidence for this mechanism occurs within the minor tennantite. The tennantite has changed from large undeformed single crystals in the starting material (B-1) (Fig. 12) to remnant ‘porphyroclast’ and ‘recrystallised grains’ in run 048 (Fig. 13). The recrystallised tennantite grains are much larger than those found in the pyrite in run 048 (Fig. 14) and are diagnostic of sub-grain rotation (SGR) recrystallisation and recovery processes (Table 3, Fig. 16). Therefore in areas of the sample where films of tennantite are present pyrite grains are likely to have slipped past one another accommodated by SGR in the tennantite. Thus, while pyrite grains in run 048 are undergoing recrystallisation via regime 1 the tennantite grains are operating in regime 2 (Fig. 16). This reflects the different conditions needed for deformation and recovery mechanisms to operate in tennantite compared with pyrite an expected result in multiphase samples where there is a significant variation in the strength of the minerals present. The similar micro-structures found within run 092 would suggest that the processes observed operating between pyrite grains at 550 °C are also expected to be occurring at 600 °C.

The two higher temperature runs; 059 (650 °C) and 053 (700 °C) are characterised by a reduction in low-angle ( $2^\circ$ ) sub-grain boundaries. This suggests that there has been a change in the deformation mechanism(s) operating as temperatures have risen to 650 °C. This reduction in dislocation density can be accounted for by two possible mechanisms (Table 3). Above 650 °C, dislocation creep may still be the dominant deformation mechanism, but recovery and recrystallisation may have become much more important at these conditions. This would result in far fewer dislocation walls being preserved within pyrite grains as they would be swept out during recovery processes. The other possibility is that with increasing temperature dislocation creep has become less important and diffusion creep has become the dominant deformation mechanism, resulting in few if any dislocation walls being formed.

Reflected light analysis suggests that grain boundaries in runs 059 and 053 are more irregular and embayed than at lower temperatures and there are fewer small ( $<10\ \mu\text{m}$ ) rounded pyrite grains present than in the low temperature runs (Fig. 15). Thus, it is most likely that as temperatures have risen above 650 °C recrystallisation mechanisms have changed from bulging (BLG) to either sub-grain rotation (SGR) or grain boundary migration (GBM) resulting in removal of most if not all of the dislocations from within pyrite grains (Fig. 15; Table 3). In run 059 (650 °C) the large pyrite grains appear very irregular and in places ribbon-shaped, and are often surrounded by clusters of smaller much more rounded pyrite grains, far larger than those found in 048 and more numerous than those in 092 (Fig. 15). This is characteristic of SGR mechanisms (Table 2, Figs. 13, 15 and 16) where texture development occurs by new recrystallised grains being developed around large remnant porphyroclasts. Therefore at 650 °C dislocation creep has still operated, as evident from dislocation walls within grains, but formation of new grains is completely analogous to regime 2 of Hirth and Tullis (1992), and SGR has removed much of the evidence for plastic deformation within original grains.

At 700 °C the microstructures developed are very different from lower temperatures. While there are still smaller grains present they are less numerous in number and grain boundaries are often curved and even lobate in places (Fig. 15). This suggests grain boundary migration (GBM) or regime 3-like deformation of Hirth and Tullis (1992) (Fig. 16). There is limited evidence for small lattice misorientations in many grains at 700 °C, and such microstructures tend to be concentrated near grain boundaries. Thus, it is likely that dislocation creep still operated at 700 °C but migration of grain boundaries has swept much of the evidence out. Thus, as temperature increases from 650 °C to 700 °C recrystallisation mechanisms also changed moving from regime 2 (SGR) to regime 3 (GBM). There is also evidence for other mechanisms operating within the higher temperature runs (059 and 053) along with dislocation creep and dynamic recrystallisation. The boundaries of some pyrite grains are very straight and have recrystallised grains running along their boundaries, presenting the possibility of grain boundary sliding. This would facilitate deformation without subsequent shape change of pyrite grains. The SGR microstructures present in the tennantite in run 048 (Fig. 13) are no longer obvious in the high temperature runs. In run 053 tennantite grains are very elongate and contain numerous dislocation walls. This suggests dislocation creep mechanisms operated and, with the lack of any obvious clusters of rounded tennantite grains, possibly grain boundary migration. Thus, grain boundary sliding is likely to have operated in discrete zones where very straight pyrite-pyrite contacts are present and also more readily along boundaries with the minor phases.

### 5.3. Intra-grain crystal orientations

All four experimentally deformed samples show at least some intra-granular pyrite lattice rotation either about  $\langle 100 \rangle$



or  $\langle 110 \rangle$  axes. The majority of deformed pyrite grains have undergone rotation about a single  $\langle 100 \rangle$  axis and this is generally shown by straight or gently curved bands in OC images. Rotation about two separate  $\langle 100 \rangle$  axes is less common and generally occurs where a pyrite grain is impinged between two or more other grains. This results in the same part of the grain rotating about different  $\langle 100 \rangle$  directions and is often identified in OC images by a checkerboard style array of sub domains. The least common type of rotation is about a single  $\langle 110 \rangle$  axis. This probably reflects the higher critical resolved shear stress (CRSS) required for its activation compared to the more common  $\langle 100 \rangle$  (Cox et al., 1981; Graf et al., 1981). It is thought to be activated when a pyrite grain in a special orientation is indented by the edge of another pyrite grain causing much higher local stresses.

#### 5.4. Whole sample crystal orientations

In many studies of mineral deformation, dislocation creep generally results in the development of a bulk-rock CPO (Fliervoet et al., 1999; Lapworth et al., 2002; Mainprice et al., 2004). However, in this study this is not the case and all of the deformed samples have a uniform (random) CPO. It has been determined by several authors that pyrite has several independent slip systems (Cox et al., 1981; Graf et al., 1981). These include principally slip on  $\{100\}$  but, as shown here and by others, slip on  $\{110\}$  is also a possibility (Boyle et al., 1998). This coupled with pyrite being a cubic mineral means that there are several combinations of 5 independent systems which may operate and so fulfil the ‘von Mises condition’ (Kelly et al., 2000). Previous studies of naturally deformed pyrite and garnet suggest that even with dislocation creep mechanisms operating a bulk CPO has either not developed or has been weak at best (Boyle et al., 1998; Storey and Prior, 2005). Studies of experimentally deformed galena do show the development of weak to moderate CPOs but not in all samples (Jansen et al., 1998). Conversely materials with high cubic symmetry such as FCC metals generate strong CPOs (Humphreys and Hatherly, 1992; Kaneno et al., 2006), but these studies involve rapid plane strain compression without dislocation creep, which is not analogous to the material in this study. Thus, in the samples analysed in this study it is likely that a combination of factors including: the number of possible independent slip systems, the conditions of experimental deformation and grain boundary sliding mechanisms have together resulted in the lack of any CPO development.

#### 5.5. Deformation mechanisms and the mechanism map

The results of this study suggest that with a constant strain rate of  $2 \times 10^{-4} \text{ s}^{-1}$  the dominant deformation mechanism operating in pyrite between temperatures of 550 °C and 700 °C is dislocation creep. As temperatures increase the style of recrystallisation and recovery changes from bulging to sub-grain rotation and finally grain boundary migration resulting in the loss of much of the evidence for dislocation creep. The minor phases while only making up about 5% of the samples show

well developed microstructures which are likely to have influenced in places how the samples have deformed, predominantly through grain boundary sliding. While these mechanisms are the dominant ones operating in the samples they are not exclusive and it is likely that in different areas there will be competition and overlap between not only these mechanisms but also diffusion creep.

The proposed deformation mechanism map for pyrite (Fig. 2) by McClay and Ellis (1983) would suggest that for a strain rate of  $2 \times 10^{-4} \text{ s}^{-1}$  at 550–600 °C the dominant deformation mechanism operating should be dislocation glide, while at 650–700 °C it would move into dislocation creep. The results presented here suggest the dislocation creep field for pyrite needs to be expanded to higher differential stresses at 550–600 °C.

## 6. Conclusions

Deformation of the samples has resulted in shape change of pyrite grains relative to the starting material (B-1). Shape change can account for most if not all of the experimental shortening in all of the samples.

At all conditions of deformation between 550 and 700 °C pyrite deforms internally by dislocation creep, mainly involving lattice rotation about  $\langle 100 \rangle$  but less commonly about  $\langle 110 \rangle$ .

At temperatures between 500 and 550 °C recovery and recrystallisation operates via grain bulging mechanisms, while at 650 °C sub-grain rotation occurs and finally grain boundary migration as temperatures reach 700 °C. Recrystallisation is more effective at high temperatures, resulting in removal by grain boundary migration of most if not all of the dislocations walls within pyrite grains.

Dislocation creep resulting in shape change of pyrite grains is the dominant mechanism operating. However, there is also evidence for dynamic recrystallisation and for grain boundary sliding accommodated by SGR in the minor phases between pyrite grains.

Different sulphides can deform by different mechanisms under the same conditions, depending upon their strength (Atkinson et al., 1977). This is observed most readily in run 048 where pyrite grains are recovering within regime 1 whereas the tennantite grains appear to be in regime 2.

## Acknowledgments

This research was carried out as part of a Ph.D. project by C.D.B. and funded by a University of Liverpool studentship. The authors gratefully acknowledge Prof. Stephen Cox and Prof. Heinrich Siemes for providing the samples used within this study. C.J. Veltkamp is thanked for help with electron microscopy. An Anonymous referee and N. Timms are also thanked for their helpful comments in reviewing this manuscript.

## References

- Allen, R.L., Weihed, P., Blandell, D., Crawford, T., Davidson, G., Galley, A., Gibson, H., Hannington, M., Herrington, R., Herzig, P., Large, R.,

- Lentz, D., Maslennikov, V., McCutcheon, S., Peter, J., Tornos, F., 2002. Global comparisons of volcanic-associated massive sulphide districts. Geological Society Special Publication 204, 13–37.
- Atkinson, B.K., 1975. Experimental deformation of polycrystalline pyrite: effects of temperature, confining pressure, strain rate and porosity. *Economic Geology* 70, 473–487.
- Atkinson, B.K., 1977. The kinetics of ore deformation: Its illustration and analysis by means of deformation mechanism maps. *Geologiska Foreningens I Stockholm Forhandlingar* 99, 186–197.
- Bestmann, M., Prior, D.J., 2003. Intragranular dynamic recrystallisation in naturally deformed calcite: diffusion accommodated grain boundary sliding as a result of subgrain rotation recrystallisation. *Journal of Structural Geology* 25, 1597–1613.
- Boyle, A.P., Prior, D.J., Banham, M.H., Timms, N.E., 1998. Plastic deformation of metamorphic pyrite: new evidence from electron backscatter diffraction and foreshorter orientation contrast imaging. *Mineralium Deposita* 34, 71–81.
- Brokmeier, H.G., 1989. Neutron diffraction texture analysis of multi-phase systems. *Textures and Microstructures* 10, 325–346.
- Cox, S.F., Etheridge, M.A., Hobbs, B.E., 1981. The experimental ductile deformation of polycrystalline and single crystal pyrite. *Economic Geology* 76, 2105–2117.
- Cox, S.F., 1987. Flow mechanisms in sulphide minerals. *Ore Geology Reviews* 2, 133–171.
- Fliervoet, T.F., Drury, M.R., Chopra, P.N., 1999. Crystallographic preferred orientations and misorientations in some olivine rocks deformed by diffusion or dislocation creep. *Tectonophysics* 303, 1–27.
- Freitag, K., Boyle, A.P., Nelson, E., Hitzman, M., Churchill, J., Lopez-Pedrosa, M., 2004. The use of electron backscatter diffraction and orientation contrast imaging as tools for sulphide textural studies: example from the greens creek deposit (Alaska). *Mineralium Deposita* 39, 103–113.
- Gill, G.E., 1969. Experimental deformation and annealing of sulphides and interpretation of ore textures. *Economic Geology* 64, 500–508.
- Graf, J.L., Skinner, B.J., 1970. Strength and deformation of pyrite and pyrrhotite. *Economic Geology* 65, 206–215.
- Graf, J.L., Skinner, B.J., Bras, J., Fagot, M., Levade, C., Couderc, J.J., 1981. Transmission electron microscopic observations of plastic deformation in experimentally deformed pyrite. *Economic Geology* 76, 38–742.
- Higgins, M.D., 2000. Measurement of Crystal size distributions. *American Mineralogist* 85, 1105–1116.
- Higgins, M.D., 2002. Closure in crystal size distributions (CSD), verification of CSD calculations and the significance of CSD fans. *American Mineralogist* 87, 171–175.
- Hirth, G., Tullis, J., 1992. Dislocation creep regimes in quartz aggregates. *Journal of Structural Geology* 14, 145–159.
- Humphreys, F.J., Hatherly, M., 1992. *Recrystallisation and Related Annealing Phenomena*. Pergamon Press. 43–52.
- Jansen, E.M., Siemes, H., Brokmeier, H.G., 1998. Crystallographic preferred orientation and microstructure of experimentally deformed Braubach galena ore with emphasis on the relation to diffusional processes. *Mineralium Deposita* 34, 57–70.
- Jansen, E.M., Siemes, H., Merz, P., Schaefer, W., Will, G., Dahms, M., 1993. Preferred orientation of experimentally deformed Mt Isa chalcopyrite ore. *Mineralogical Magazine* 57, 45–53.
- Kaneno, Y., Takahashi, A., Takasugi, T., 2006. Microstructure and texture evolution during cold rolling and annealing of Ni<sub>3</sub>Fe alloy. *Materials science and Engineering* 431, 328–338.
- Kelly, A., Groves, G.W., Kidd, P., 2000. *Crystallography and Crystal Defects*, revised ed. John Wiley and Sons, 196–197.
- Lapworth, T., Wheeler, J., Prior, D.J., 2002. The deformation of plagioclase investigated using electron backscatter diffraction crystallographic preferred orientation data. *Journal of Structural Geology* 24, 387–399.
- Levade, C., Couderc, J.J., Bras, J., Fagot, M., 1982. Transmission electron microscopy study of experimentally deformed pyrite. *Philosophical Magazine* 46, 307–325.
- Mainprice, D., Bascou, J., Cordier, P., Tommasi, A., 2004. Crystal preferred orientations of garnet: comparison between numerical simulations and electron back-scattered diffraction (EBSD) measurements in naturally deformed eclogites. *Journal of Structural Geology* 26, 2089–2102.
- McClay, K.R., Ellis, P.G., 1983. Deformation and recrystallization of pyrite. *Mineralogical Magazine* 47, 527–538.
- McClay, K.R., Ellis, P.G., 1984. Deformation of pyrite. *Economic Geology* 79, 400–403.
- Michibayashi, K., Mainprice, D., 2004. The role of pre-existing mechanical anisotropy on shear zone development within oceanic mantle lithosphere: an example from the Oman ophiolite. *Journal of Petrology* 45, 405–414.
- Ohfuji, H., Boyle, A.P., Prior, D.J., Rickard, D., 2005. Structure of framboidal pyrite: an electron backscatter diffraction study. *American Mineralogist* 90, 1693–1704.
- Passchier, C.W., Trouw, R.A.J., 2005. In: *Microtectonics*, second ed. Springer, pp. 40–51.
- Prior, D.J., Trimby, P.W., Weber, U.D., Dingley, D.J., 1996. Orientation contrast imaging of microstructures in rocks using foreshorter detectors in the scanning electron microscope. *Mineralogical Magazine* 60, 859–869.
- Prior, D.J., Boyle, A.P., Brekner, F., Cheadle, M.C., Day, A., Lopez, G., Peruzzo, L., Potts, G.J., Reddy, S., Spiess, R., Timms, N.E., Trimby, P., Wheeler, J., Zetterström, L., 1999. The application of electron backscatter diffraction and orientation contrast imaging in the SEM to textural problems in rocks. *American Mineralogist* 84, 1741–1759.
- Prior, D.J., Wheeler, J., Peruzzo, L., Spiess, R., Storey, C., 2002. Some garnet microstructures: an illustration of the potential of orientation maps and misorientation analysis in microstructural studies. *Journal of Structural Geology* 24, 999–1011.
- Ramdohr, P., 1969. *The Ore Minerals and their Intergrowths*. International Series of Monographs on Earth Sciences. Pergamon Press.
- Siemes, H., Zilles, D., Cox, S.F., Merz, P., Schaefer, W., Will, G., Schaeben, H., Kunze, K., 1993. Preferred orientation of experimentally deformed pyrite by means of neutron diffraction. *Mineralogical Magazine* 57, 29–43.
- Storey, C.D., Prior, D.J., 2005. Plastic deformation and recrystallization of garnet: a mechanism to facilitate diffusion creep. *Journal of Petrology* 46, 2593–2613.
- Van Goethem, L., Van Landuyt, J., Amelinckx, S., 1978. Study of the glide elements in pyrite by means of electron microscopy and electron diffraction. *American Mineralogist* 63, 548–550.
- Wheeler, J., Prior, D.J., Jiang, Z., Spiess, R., Trimby, P.W., 2001. The petrological significance of misorientations between grains. *Contributions to Mineralogy and Petrology* 141, 109–124.